Journal Pre-proofs

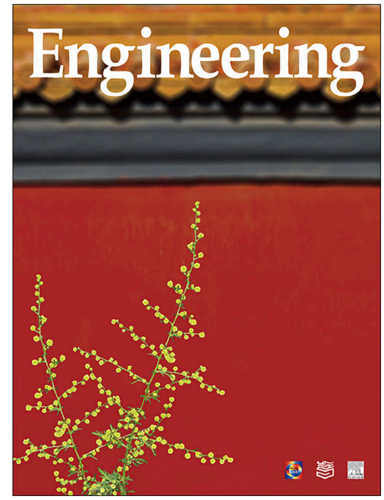

Article

Experimental Investigation on Thermoacoustic and Structural Dynamics in a Premixed Arrayed Micro-Tube Hydrogen Combustor

Xiao Han, Ziyu Qin, Yuzhen Lin, Yunxin Chang, Juan Guzmán-Iñigo, Chi Zhang

PII: S2095-8099(26)00323-1
DOI: https://doi.org/10.1016/j.eng.2026.04.017
Reference: ENG 2350

To appear in: *Engineering*

Received Date: 27 August 2025
Revised Date: 31 March 2026
Accepted Date: 26 April 2026

Please cite this article as: X. Han, Z. Qin, Y. Lin, Y. Chang, J. Guzmán-Iñigo, C. Zhang, Experimental Investigation on Thermoacoustic and Structural Dynamics in a Premixed Arrayed Micro-Tube Hydrogen Combustor, *Engineering* (2026), doi: https://doi.org/10.1016/j.eng.2026.04.017

Research

Green Aviation Propulsion—Article

Experimental Investigation on Thermoacoustic and Structural Dynamics in a Premixed Arrayed Micro-Tube Hydrogen Combustor

Xiao Han[a,b] , Ziyu Qin[a,b,c] , Yuzhen Lin[a,b,*], Yunxin Chang[a,b] , Juan Guzmán-Iñigo[d] , Chi Zhang[a,b]

[a] *National Key Laboratory of Science and Technology on Aero-Engine Aero-thermodynamics, Research Institute of Aero-Engine, Beihang University, Beijing 100191, China*

[b] *Collaborative Innovation Center for Advanced Aero-Engine, Beihang University, Beijing 100191, China*

[c] *Shenyuan Honors College, Beihang University, Beijing 100191, China*

[d] *Department of Engineering, City St George's, University of London, London EC1V 0HB, UK*

*Corresponding Author.

Email address: linyuzhen@buaa.edu.cn (Y. Lin)

Abstract

Thermoacoustic instability remains a major challenge in the development of hydrogen micromix combustors. This study presents the design of a full-scale premixed-array microtube hydrogen combustor. Jet-in-crossflow micromixing technology was employed, resulting in relatively uniform mixing within each injector tube. Subsequently, the thermoacoustic dynamics were investigated. A low-order thermoacoustic model was used to characterize the experimentally observed longitudinal acoustic oscillations, with a deviation of 1.6% in the predicted modal frequency. After the onset of thermoacoustic instability, intermittent high-amplitude burst oscillations emerged amid low-amplitude combustion noise at moderate equivalence ratios, as quantified using recurrence quantification metrics. As the equivalence ratio increased further, the bursts gradually dominated the pressure fluctuations, eventually leading to an intense limit-cycle oscillation above 1800 Pa. Collective synchronization among individual flames was a key factor in distinguishing intermittent from limit-cycle oscillations. The phase difference between the heat-release fluctuations of different flame elements was nearly fixed during limit-cycle oscillation, whereas intermittent oscillation showed weaker phase synchronization. Finally, the structural vibration induced by thermoacoustic oscillations was found to be spatially anisotropic and to exhibit a linear amplitude relationship. The derived proportional coefficient was 8.5 $m\cdot(s^2\cdot kPa)^{-1}$, which facilitates quantitative evaluation of the strength of thermoacoustically induced vibration. The structural dynamics exhibited a significant response gain in the high-frequency regime. This study sheds light on understanding the instability and broadening the operability of the hydrogen combustor.

Keywords: Hydrogen micromix combustor, Thermoacoustic instability, Intermittency, Structural vibration

1. Introduction

The global energy architecture is experiencing a profound decarbonization transition [1], in which hydrogen gas turbines are expected to play a crucial role. This importance arises not only from their potential for zero-carbon emissions but also from their ability to enable the flexible use of intermittent renewable energy sources (e.g., wind and solar power) through a power-to-hydrogen-to-power pathway [2]. However, the unique properties of hydrogen, such as its higher flame speed and burning temperature relative to hydrocarbon fuels, increase the risks of flashback and excessive nitrogen oxide emissions [2,3]. Consequently, traditional burner configurations specifically designed for hydrocarbon fuels are unsuitable for pure hydrogen combustion.

To address these technical challenges, the conventional large-scale flame configuration has been replaced with a cluster of mesoscale flames to increase jet velocity and reduce residence time by decreasing injector size. The core design principle of this multi-injector combustor centers on the mixing of hydrogen and air within each injector.

Funke et al. [4,5] reviewed a jet-in-crossflow mixing configuration in which hydrogen was injected perpendicularly into the axial airflow at the injector exit. This micromix technology was successfully validated in an industrial full-scale can-level combustor and demonstrated low-emission performance. Another industrial gas turbine application featuring lean direct injection with a similar crossflow mixing strategy was reported in Ref. [6]. York et al. [7] employed jet-in-crossflow micromixing in numerous injectors and designed a specialized premixing zone within each injector, which facilitated relatively uniform mixing. Weida et al. [8] employed coaxial jet mixing, in which each fuel tube was surrounded by three air-injection lobes. Several laboratory-scale multi-injector micromix burners with high fuel flexibility have also been investigated, including a 4 × 4 array layout [9,10] and a concentric circular layout [11,12]. Overall, flexible micromixing has been widely adopted as an effective strategy for hydrogen combustion.

Despite progress in addressing flashback and emission issues, thermoacoustic instability [13], which arises from coupling between system acoustics and unsteady flame heat release, remains a major challenge in hydrogen combustors, particularly under micro-premixed combustion conditions. Although thermoacoustic instability has been extensively studied in hydrocarbon swirl flames [14–16], it remains insufficiently understood in arrayed hydrogen flames. From the standpoint of qualitative flame dynamics visualization, Lee and Kim [17] found that distributed hydrogen flames exhibit a stronger tendency toward higher-order modes and more independent motion among constituent flames than methane flames. Furthermore, Kang and Kim [18] examined three types of flame motion corresponding to three acoustic modes. Durocher et al. [19] explored flame evolution during an acoustic cycle using a novel three-dimensional (3D) measurement approach, highlighting complex flame–flame interactions. From the standpoint of quantitative flame response modeling represented by the flame transfer function (FTF), Æsøy et al. [20] and Garcia et al. [21] reported experimental and numerical results, respectively, and concluded that hydrogen addition increases the cutoff frequency from the gain curves and decreases the time delay from the phase curves. The FTFs of pure hydrogen flames were also measured in a micromix multi-injector combustor, confirming low-pass filter behavior [10,22]. In summary, the unique properties of compact hydrogen flames give rise to hydrogen-specific thermoacoustic dynamics.

From the perspective of macroscopic dynamics, thermoacoustic instability can develop through multiple pathways. The existing literature has shown that intermittency is a distinct dynamic state along the route to thermoacoustic instability. Guan et al. [23] observed a transitional intermittent state in a self-excited thermoacoustic system with a laminar premixed flame while continuously adjusting flame position. Nair et al. [24] identified intermittency during the transition to thermoacoustic oscillation in both swirl-stabilized and bluff-body-stabilized turbulent combustors, using flow Reynolds number as the bifurcation parameter. Additional related studies have been reported [25,26]. However, it remains unclear whether this transition route also exists in the novel hydrogen micromix configuration, given its distinctive flame dynamics. To address this gap, we aim to provide direct experimental evidence of this intermittency and to deepen understanding of the dynamic characteristics of hydrogen micromix combustors.

Special thermoacoustic dynamics are often interpreted using nonlinear reduced-order dynamic models with a stochastic noise term. For example, Bonciolini et al. [27] developed a nonlinear stochastic van der Pol (VdP) model with distributed, correlated time delays to account for thermoacoustic intermittency. Bhavi et al. [28] employed a modified stochastic VdP model featuring higher-order nonlinearity, which effectively captures the secondary abrupt subcritical bifurcation. In addition, Lee [29] utilized a coupled stochastic VdP model to investigate lock-in between two thermoacoustic oscillators.

Additionally, high-amplitude pressure oscillations act as a detrimental excitation source, often inducing structural vibrations in the engine and even leading to catastrophic damage [30]. Despite their practical importance, thermoacoustically induced vibrations have not received sufficient attention. To simulate this phenomenon, Pozarlik and Kok [31] and Shahi et al. [32] used explicit and implicit partitioned acoustic-structure coupling numerical algorithms, respectively. Both methods involve two separate computational fluid dynamics and computational structural dynamics solvers to simulate thermoacoustic oscillations and structural vibrations, respectively, with iterative information exchange at the acoustic-structure interface. Furthermore, Xia et al. [33] employed an advanced approach that integrated thermoacoustic and structural dynamics computations into a single solver. These simulation approaches successfully reproduced several experimental phenomena and revealed the acoustic-structure coupling mechanism, although at relatively high computational cost. In addition, existing experimental studies have mostly focused on idealized configurations.

Can Altunlu et al. [34] investigated a laboratory-scale bluff-body-stabilized burner and measured wall vibration velocity using a laser Doppler vibrometer. They demonstrated that structural vibrations are sensitive to excitation by higher-order acoustic modes. Rubio-Rubio et al. [35] utilized a simple Hele-Shaw chamber to measure the acceleration signal of a chamber plate. The induced vibrations were found to suppress thermoacoustic instability. In addition, in our previous work [36], we established a nonlinear dynamic model relating injector acceleration to pressure fluctuations, thereby scaling the experimental results over a wide operating range. However, vibration directionality was not examined because only one acceleration measurement point was used. In this study, we aimed to gain deeper insight into thermoacoustically induced vibrations by integrating multidimensional signals.

In this study, we designed a realistic full-scale premixed-array microtube hydrogen combustor with jet-in-crossflow micromixing. The dynamics of both thermoacoustic oscillations and structural vibrations were investigated.

The remainder of this paper is organized as follows. Section 2 describes the experimental setup. Section 3 introduces the modeling and data-processing methods. Sections 4 and 5 discuss the thermoacoustic dynamics in the frequency and time domains, respectively, to provide a comprehensive understanding. Specifically, Sections 5.1 and 5.2 expound on the acoustic-pressure and flame dynamics, respectively. Finally, Section 6 analyzes the structural vibration characteristics induced by thermoacoustic instability.

2. Experimental setup

In this study, we developed a full-scale premixed-array microtube (P-AMT) combustor for hydrogen operation, as shown in Fig. 1. The burner featured a centrally staged layout consisting of an inner pilot stage and an outer main stage. A typical swirl-cup configuration (Fig. 1(f)) for flame stabilization was adopted for the pilot stage. Hydrogen was mixed with two streams of swirled airflow downstream of the injector. In contrast to a conventional hydrocarbon combustor, which uses a single large-scale annular swirl injector, the main stage of the hydrogen combustor employed in this study comprised 29 microtube injectors to enhance flashback resistance. The injectors were arranged in three groups in a concentric hexagonal layout. To facilitate flexible load adjustment, these main-stage injectors were divided into first- and second-stage injectors. Six injectors in the main stage (denoted by purple circles in Fig. 1(c)) served as second main-stage injectors, whereas the other 23 injectors (denoted by green circles in Fig. 1(c)) served as first main-stage injectors. For each main-stage injector (Fig. 1(g)) with an inner diameter of 12.6 mm, hydrogen entered the microtube through four holes with a diameter of 0.8 mm and mixed with air along the injector. A twisted vane and a flow straightener were placed inside the microtube to promote mixing and achieve uniform flow. Based on preliminary simulations, the main-stage flame was considered premixed.

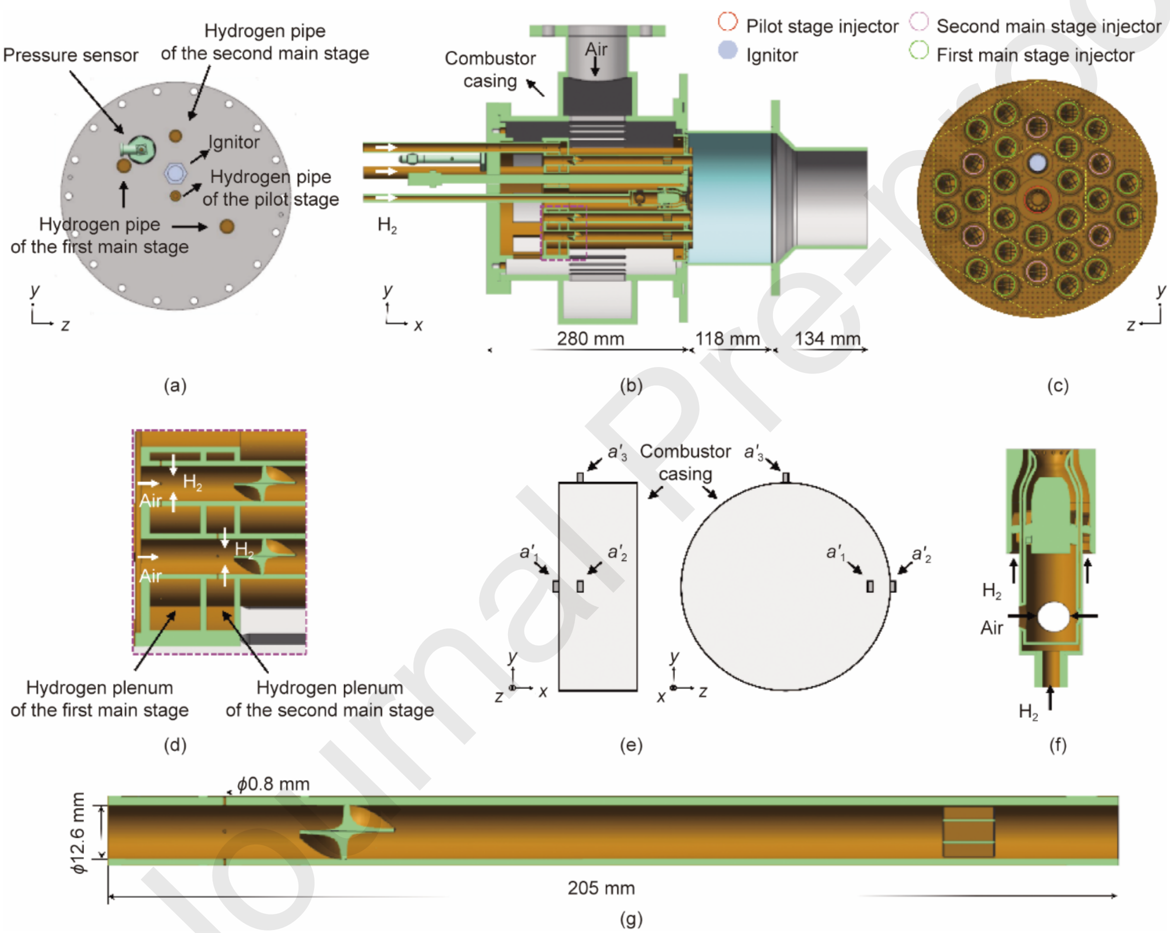

Fig. 1 Schematic of the hydrogen arrayed multi-nozzle combustor. (a) Left view. (b) Section view. (c) Right view. (d) Local zoom view. (e) Accelerometer position (acceleration fluctuations $a_1^{'}$, $a_2^{'}$, and $a_3^{'}$ represented structural vibrations along the x, z, and y directions, respectively). (f) Pilot stage injector. (g) Main stage injector.

The experiments were conducted under atmospheric conditions. Air flowed into the combustor through the sidewall and was then distributed to the pilot stage and the first- and second-stage main injectors according to their effective area ratios. The total air mass flow rate was controlled using an electric control valve (adjustable range 50–350 $g \cdot s^{-1}$, 0.5% full-scale accuracy). Hydrogen entered the combustor through multiple inlet pipes, as shown in Fig. 1(a). Hydrogen supplied to the first and second main stages was directed into two separate plenums and injected into the microtubes through holes in the wall, as depicted in Fig. 1(d). The hydrogen mass flow rates of the pilot stage and the first and second main stages were controlled independently by three mass flow controllers (Beijing Accuflow Technology Co, Ltd., China, 0.5% full-scale accuracy), with adjustable ranges of 0–800, 0–300, and 0–1500 standard liters per minute (SLM), respectively. Downstream of the injectors was a quartz glass tube for flame visualization, followed by an exhaust tube after a slight contraction section. Pressure fluctuations inside the air plenum were recorded using a pressure sensor (112A22, PCB Piezotronics, Inc., USA, 14.5 mV·kPa^{-1}, 1% uncertainty). The vibration accelerations of the combustor casing along three directions were measured by three accelerometers welded onto the casing (CA-YD-182, Sinocera Piezotronics, Inc., China, 2 mV·(m·s^{-2})$^{-1}$ sensitivity), as shown in Fig. 1(e). Acceleration fluctuations a_1', a_2', and a_3' represented structural vibrations along the x, z, and y directions, respectively. The pressure sensor and accelerometers were calibrated using standard acoustic pressure and vibration signals, respectively. Pressure and acceleration signals were acquired simultaneously at 20 kHz.

The operating conditions are listed in Table 1. The total air mass flow rate $\dot{m}_\mathrm{a}$, was set to 160 g·s^{-1}, corresponding to a bulk flow velocity of U_b = 48.7 m·s^{-1}. The equivalence ratio, ϕ, ranged from 0.325 to 0.425 in increments of 0.02, corresponding to a thermal power (P) range of 181–237 kW. The equivalence ratio of the pilot stage (ϕ_p= 0.451) and the staging ratio between the first and second main stage ($\phi_{\mathrm{m},1}/\phi_{\mathrm{m},2} = 1$) are fixed. A uniform equivalence ratio distribution between the two stages was expected to promote thermoacoustic instability, whereas an asymmetric equivalence ratio distribution between the two stages tends to attenuate oscillation amplitude, as reported for a stratified swirl burner [37] and an arrayed multi-nozzle burner [12]. The hydrogen mass flow rates of the first and second main stages, $\dot{m}_{\mathrm{f,m},1}$ and $\dot{m}_{\mathrm{f,m},2}$, are adjusted accordingly. The hydrogen jet velocities exiting the pilot- and main-stage holes were approximately 76 and 300 m·s^{-1}, respectively.

Table 1
Experimental operating conditions.

	$\dot{m}_\mathrm{a}$ (g·s^{-1})	U_b (m·s^{-1})	ϕ	ϕ_p	$\phi_{\mathrm{m},1}$	$\phi_{\mathrm{m},2}$	$\dot{m}_\mathrm{f,p}$ (g·s^{-1})	$\dot{m}_{\mathrm{f,m},1}$ (g·s^{-1})	$\dot{m}_{\mathrm{f,m},2}$ (g·s^{-1})	P (kW)
1	160	48.7	0.325	0.451	0.418	0.418	0.093	1.122	0.293	181
2	160	48.7	0.345	0.451	0.445	0.445	0.093	1.195	0.312	192
3	160	48.7	0.365	0.451	0.472	0.472	0.093	1.269	0.331	203
4	160	48.7	0.385	0.451	0.500	0.500	0.093	1.342	0.350	214
5	160	48.7	0.405	0.451	0.527	0.527	0.093	1.416	0.369	225
6	160	48.7	0.425	0.451	0.554	0.554	0.093	1.490	0.389	237

3. Methodology

3.1. Low-order thermoacoustic model

To construct a thermo-acoustic model that aims to reveal the unstable mode, we employed the following acoustic Riemann invariants:

$$A^+ = \frac{1}{2}\left(p' + \rho c u'\right) \quad (1)$$

$$A^- = \frac{1}{2}\left(p' - \rho c u'\right) \quad (2)$$

where A^+ and A^- represent the downstream and upstream propagating waves, respectively. p', u', ρ, c denote the pressure fluctuation, velocity fluctuation, gas density, and sound speed, respectively. The upstream inlet boundary invariants A_u^+,A_u^- and downstream outlet boundary invariants A_d^+,A_d^- are related by multiplying a series of transfer matrices, which leads to the following formulation:

$$\begin{pmatrix} A_\mathrm{d}^+ \\ A_\mathrm{d}^- \end{pmatrix} = \begin{pmatrix} M_{11} & M_{12} \\ M_{21} & M_{22} \end{pmatrix} \begin{pmatrix} A_\mathrm{u}^+ \\ A_\mathrm{u}^- \end{pmatrix} \quad (3)$$

Among these matrices, the transfer matrix linking the invariants upstream and downstream of the flame is given by:

$$\boldsymbol{M}_\mathbf{f} = \frac{1}{2}\begin{pmatrix} 1 + \Gamma(1 + \theta F(\omega)) & 1 - \Gamma(1 + \theta F(\omega)) \\ 1 - \Gamma(1 + \theta F(\omega)) & 1 + \Gamma(1 + \theta F(\omega)) \end{pmatrix} \quad (4)$$

where $\Gamma = (S_1/S_2)(\rho_2 c_2/\rho_1 c_1)$ is the acoustic coupling factor (S represents the cross sectional area) [38,39], $\theta = T_2/T_1 - 1$ is the dimensionless temperature rise across the flame, and $F(\omega)$ is the FTF and quantifies the effect of unsteady heat release on thermoacoustic instability.

The acoustic boundary condition is quantified by the reflection coefficient (R), which relates the upstream and downstream propagating waves as follows:

$$R_{\mathrm{u}}(\omega) = \frac{A_{\mathrm{u}}^{+}}{A_{\mathrm{u}}^{-}},(5)$$

$$R_{\mathrm{d}}(\omega) = \frac{A_{\mathrm{d}}^{-}}{A_{\mathrm{d}}^{+}}(6)$$

Combining Eqs. (3), (5), and (6), the eigenfrequency is obtained by solving the following dispersion equation:

$$R_{\mathrm{u}}R_{\mathrm{d}}M_{11} - R_{\mathrm{u}}M_{21} + R_{\mathrm{d}}M_{12} - M_{22} = (7)$$

The real and imaginary parts of the solution to Eq. (7) represent the modal frequency f and growth rate σ, respectively.

In summary, analytical investigation of thermoacoustic instability within the above framework requires the frequency-dependent functions $F(\omega)$,$R_{\mathrm{u}}(\omega)$,and $R_{\mathrm{d}}(\omega)$ are needed and will be specified for the adopted P-AMT setup in Section 4.

3.2. Nonlinear dynamics analysis

The dynamic characteristics of pressure fluctuations are studied in phase space.

The pressure fluctuation is converted into a trajectory in the reconstructed phase space using an appropriate time delay τ_{p} and embedding dimension d [40], formulated as

$$\{p_i^{'}\}_{i=1,2,\cdots,N} \rightarrow \left\{\boldsymbol{P_j} = \left(p_j^{'},p_{j+\tau_{\mathrm{p}}}^{'},\cdots,p_{j+(d-1)\tau_{\mathrm{p}}}^{'}\right)\right\}_{j=1,2,\cdots,N^{'}}(8)$$

The original signal $\{p_i^{'}\}$ contains N points. The reconstructed phase portrait $\{\boldsymbol{P_j}\}$ contains $N^{'} = N - (d-1)\tau_{\mathrm{p}}$ points, where each $\boldsymbol{P_j}$ represents a d-dimensional vector. The false nearest neighbors method [41] is used to determine the embedding dimension. A 3D phase space is often appropriate and facilitates visualization of phase portraits.

To visualize the subtle periodic behavior of the phase portrait, a recurrence plot [42] is defined as

$$\mathrm{RP}_{ij}(\varepsilon) = \Theta\left(\varepsilon - \|\boldsymbol{P_i} - \boldsymbol{P_j}\|\right) = \begin{cases} 1, \|\boldsymbol{P_i} - \boldsymbol{P_j}\| \le \varepsilon \\ 0, \|\boldsymbol{P_i} - \boldsymbol{P_j}\| > \varepsilon \end{cases}(9)$$

where Θ is the Heaviside function, $\|\cdot\|$is the Euclidean distance, and ε is the distance threshold. The threshold is used to determine whether a pair of points $(\boldsymbol{P_i},\boldsymbol{P_j})$ is close in phase space. The recurrence plot, therefore, consists of black ($\mathrm{RP}_{ij}(\varepsilon) = 1$, pairwise distance less than ε) and white ($\mathrm{RP}_{ij}(\varepsilon) = 0$, pairwise distance greater than ε) dots. To obtain a representative recurrence plot, a distance threshold equal to 10% of the attractor diameter was selected.

Furthermore, we used three quantitative metrics to reveal the intrinsic structure of the recurrence plot and to gain a more comprehensive understanding of the time-domain dynamic characteristics. First, the recurrence rate $\mathrm{RR}(\Delta,\varepsilon)$ is given by:

$$\mathrm{RR}(\Delta,\varepsilon) = \frac{1}{N^{'} - \Delta}\sum_{i=1}^{N^{'}-\Delta}\mathrm{RP}_{i,i+\Delta}(\varepsilon)(10)$$

where Δ is the diagonal line offset relative to the main diagonal line. The recurrence rate ranges from 0 to 1 and measures the occupation rate of the black dots along the diagonal line with an offset Δ.

Second, the global recurrence rate $S(\varepsilon)$ involving all the diagonal lines is calculated as

$$S(\varepsilon) = \frac{2}{N^{'}(N^{'} - 1)}\sum_{1\le i<j\le N^{'}}\mathrm{RP}_{ij}(\varepsilon)(11)$$

Then, the correlation dimension of the phase portrait is defined as

$$D = \frac{\mathrm{d}\left(\log S(\varepsilon)\right)}{\mathrm{d}\left(\log \varepsilon\right)}(12)$$

which is the slope between $S(\varepsilon)$ and ε in a logarithmic coordinate [43,44]. The correlation dimension D quantifies the topological properties of the phase portrait. If the phase portrait exhibits self-similar fractal characteristics, the global recurrence rate is expected to follow a power scaling law $S(\varepsilon) \sim \varepsilon^{D}$ for moderate threshold values.

Third, we focused on the statistical properties of the distribution of black-stripe lengths. The number C of black stripes with length l along all the diagonal lines of the recurrence plot is formulated as [45]

$$C(l,\varepsilon) = \sum_{i,j}\mathrm{RP}_{i-1,j-1}(\varepsilon)\mathrm{RP}_{i+l,j+l}(\varepsilon)\prod_{k=0}^{l-1}\mathrm{RP}_{i+k,j+k}(\varepsilon)(13)$$

Then, the average length $l_0(\varepsilon)$ is determined by:

$$l_0(\varepsilon) = \frac{\sum_{l=l_{\min}}^{N'-1} lC(l,\varepsilon)}{\sum_{l=l_{\min}}^{N'-1} C(l,\varepsilon)} \quad (14)$$

where the threshold $l_{\min}$ is taken as 19 in this study.

The above three recurrence quantification metrics—recurrence rate RR, correlation dimension D, and average length l_0 —are adopted in Section 5.1.

4. Thermoacoustic dynamics in the frequency domain

Fig. 2(a) shows the power spectral density of the pressure fluctuations under all operating conditions. A predominant peak at approximately 500 Hz gradually emerged as the equivalence ratio increased, as indicated by the green-shaded band. The peak amplitude A_p abruptly increased from 26 to 383 Pa when the equivalence ratio changed from 0.345 to 0.365, as shown in Fig. 2(b), indicating bifurcation and the onset of thermoacoustic instability. Thereafter, the instability intensity continued to increase, reaching an amplitude of 1872 Pa (equivalent to 1.85% of the mean pressure) at $\phi = 0.425$. These results show that the combustor is prone to thermoacoustic instability under high-power loads. Moreover, Figs. 2(a) and (c) demonstrate that the peak shifted to higher frequencies at higher equivalence ratios, which stemmed from the increase in burning temperature and, consequently, the increase in sound speed.

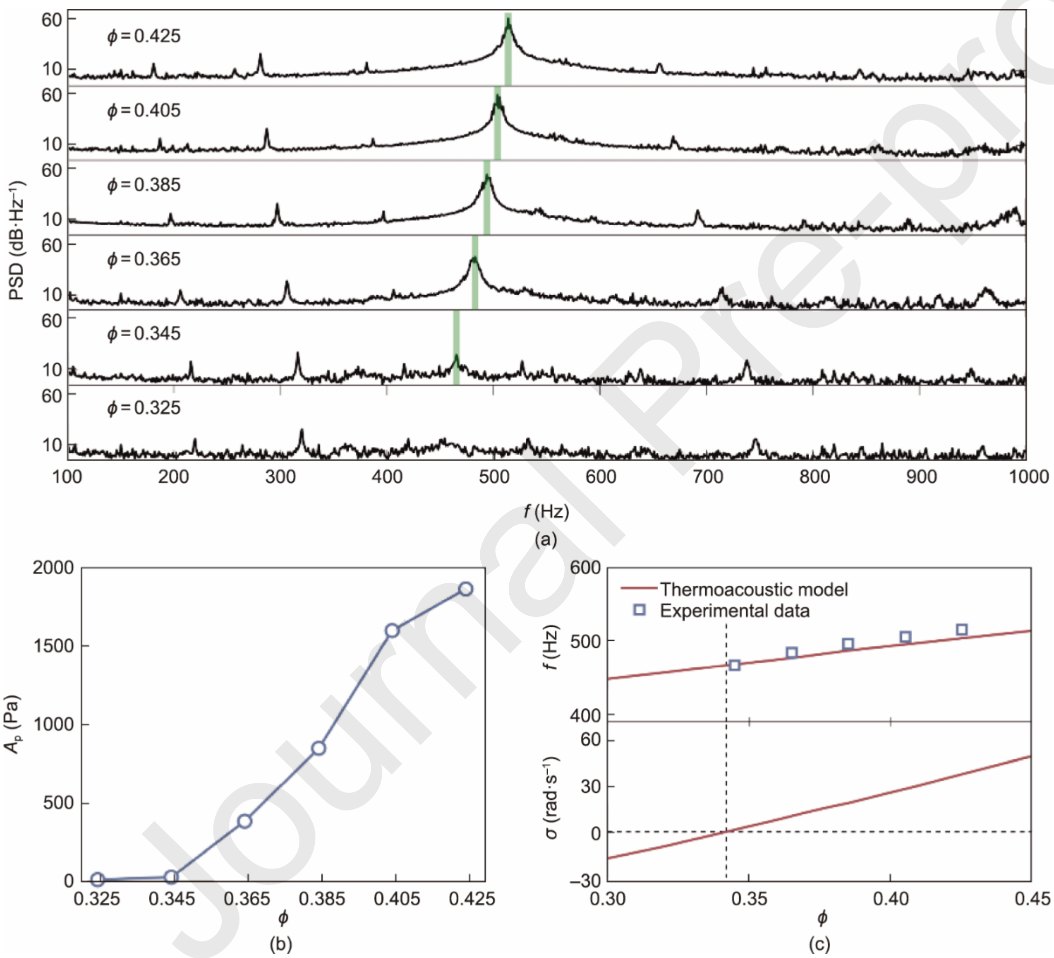

Fig. 2 (a) Power spectral density. (b) Amplitude dependency on equivalence ratio. (c) Modal frequency and growth rate predicted by the low-order thermoacoustic model and experimental frequency.

We employed the aforementioned low-order thermoacoustic model described in Section 3.1 to reproduce and analyze the observed phenomena. The model geometry is illustrated in Fig. 3(a), where the microtube ensemble is treated as an equivalent cavity with the same cross-sectional area. The contraction section was approximated by 10 straight cavities with linearly decreasing diameters.

The burning temperature in the combustion chamber was estimated as 90% of the adiabatic flame temperature (e.g., $T_\mathrm{b} = 0.9\ T_\mathrm{ad} = 1211$ K for $\phi = 0.365$) to account for wall heat loss [10].

The FTF $F(\omega)$ of the conical flame can be represented as a delayed first-order filter [46]

$$F(\omega) = \frac{\omega_c}{\omega_c - i\omega} n e^{i\omega\tau}. (15)$$

The time delay τ [47] and cutoff frequency ω_c [48] are respectively given by:

$$\tau = \frac{H}{3U_b}(1 + \cos^{-2}\alpha) (16)$$

$$\omega_c = \frac{3U_b}{r_{mt}} \sin\alpha\cos (17)$$

where α is the flame half-cone angle, H is the flame height, and r_{mt} is the microtube radius. The flame height was estimated from the flame images. The gain n was taken as 1 from the low-frequency limit of the FTF [49]. Although the FTF formulation in Eq. (15) and the parameter estimation equations, Eqs. (16) and (17), were derived for laminar flames, laminar and turbulent flames share similar large-scale disturbed flame motions. Moreover, a recent study [10] on the FTF of turbulent hydrogen-premixed arrayed flames showed a trend comparable to that described by Eq. (15). We will later show that turbulence-induced parameter modifications have a limited effect on thermoacoustic instability.

The microtube and chamber were open to the atmosphere and the plenum, respectively, resulting in approximate pressure-release acoustic boundary conditions at the inlet and outlet. Furthermore, a more accurate correction of the reflection coefficient, accounting for acoustic radiation loss at the boundary, was employed [50] as follows:

$$R(\omega) = -\left(1 - \frac{1}{2}\left(\frac{\omega r}{c}\right)^2\right) e^{1.22 i\omega r/c} (18)$$

where r is the cavity radius and c is the sound speed.

By substituting the FTF into Eq. (15) and the reflection coefficient into Eq. (18) and then solving the dispersion equation in Eq. (7), the modal frequency, growth rate, and mode shape can be obtained. As shown in Fig. 2(c), the model reproduced the frequency well, with an average deviation of 1.6% relative to the experimental data. The prediction deviation may arise because the actual oscillation is not the assumed harmonic oscillation, as explained in detail in Section 5.1. The critical equivalence ratio at which the growth rate became zero also coincided with the experimentally observed bifurcation point. In addition, Fig. 3 shows that the first-order acoustic mode was excited. The flame was located near the acoustic pressure antinode, implying strong thermoacoustic coupling according to the Rayleigh criterion [51] and, therefore, a propensity for thermoacoustic instability [17].

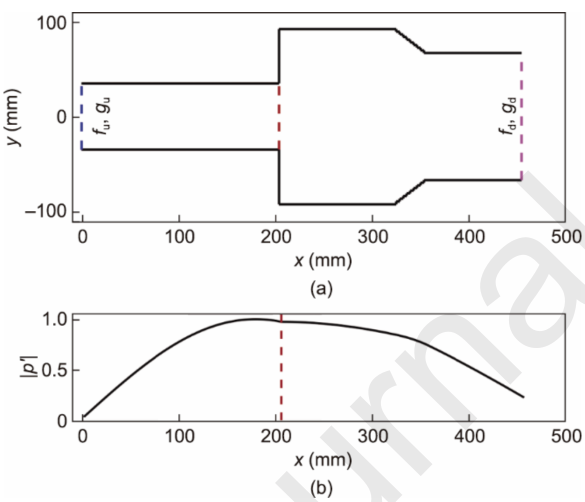

Fig. 3 (a) Geometry of the low-order thermoacoustic model. (b) Normalized modal amplitude of the acoustic pressure.

Because several parameters in the thermoacoustic model were estimated, uncertainty quantification was necessary to evaluate the robustness of the model predictions. Uncertainty in parameter estimation arises from measurement uncertainty (e.g., flame height) and unresolved processes (e.g., turbulence and heat loss). To this end, a Monte Carlo simulation with 1000 samples was conducted, in which ±5% perturbations were independently imposed on four model input parameters: burning temperature T_b, cutoff frequency ω_c, time delay τ, and gain n. The resulting frequencies and growth rates are shown in Fig. 4. The frequency uncertainty was approximately ±10 Hz. For $\phi = 0.365$ in Fig. 4(a), the growth rate for a small fraction of the samples was less than zero, although the model with unperturbed parameters predicted this condition to be unstable. We therefore judged this operating condition to be unstable, with a confidence level of 88.7%. For $\phi = 0.405$ in Fig. 4 (b), the growth rates for all samples were greater than zero, suggesting that the model prediction was robust.

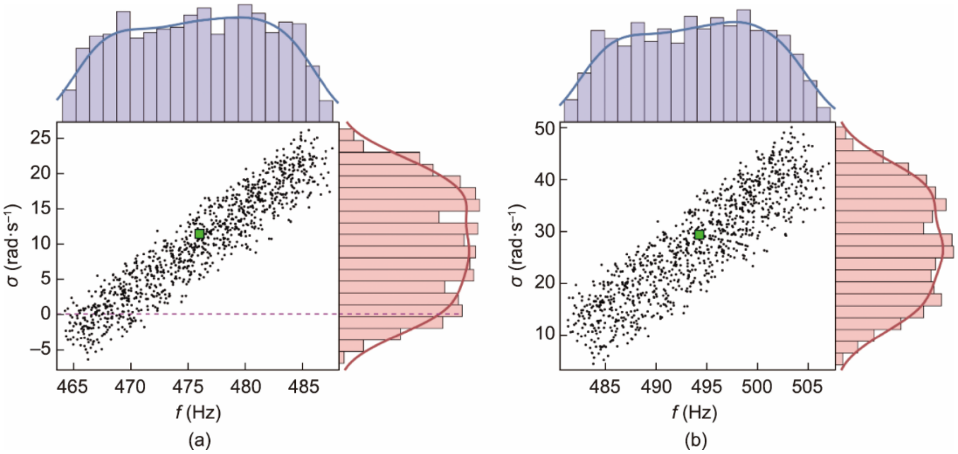

Fig. 4 Monte Carlo simulation for the thermoacoustic model. The probability density distribution of the frequency and growth rate is shown in blue and red, respectively. The green square dot denotes the model prediction with the unperturbed parameter value. (a) $\phi = 0.365$; (b) $\phi = 0.405$.

5. Thermoacoustic dynamics in the time domain

The frequency-domain analysis, which lacks temporal resolution, does not reveal the full panorama of thermoacoustic instability. To gain further insight, we investigated the dynamic characteristics of thermoacoustic oscillation in the time domain, with particular emphasis on the instability transition pathway as the equivalence ratio increases.

5.1. Acoustic pressure dynamics

Three distinct oscillation regimes were identified based on the temporal behavior of the pressure fluctuations, as evidenced by the time series, phase portraits, and recurrence plots.

In Regime 1, at low equivalence ratios, the low-amplitude pressure fluctuation (marked in pink in Fig. 5), characterized by a narrow and sharp probability density function (PDF), corresponds to the state preceding thermoacoustic instability. The phase portrait was confined to a small region around the origin in phase space, as shown in Fig. 6(a). The irregular global recurrence plot is presented in Fig. 6(b). The locally magnified recurrence plot in Fig. 6(c) further reveals a cluster of incoherent structures. Therefore, the pressure fluctuation lacked intrinsic coherence, as also confirmed by the broadband spectrum in Fig. 2(a). We classify this dynamic state as a stochastic oscillation.

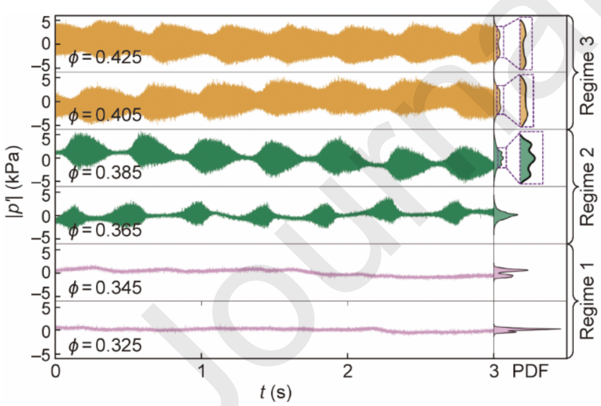

Fig. 5 Time series and associated probability density function (PDF) distribution of various equivalence ratios.

In Regime 2, at moderate equivalence ratios, the alternating occurrence of high-amplitude bursts and low-amplitude oscillations emerged as a prominent characteristic (marked in green in Fig. 5), indicating the predominance of intermittency. The PDF bulges around the zero value of p'. Specifically, a three-peak distribution was observed at $\phi = 0.385$. The solid-phase portrait in Fig. 6(a) shows distinct oscillatory behavior. The recurrence plot revealed the underlying multiscale characteristics. The global recurrence plot in Fig. 6(b), which contains alternating black and white patches, indicates a slow-varying time scale T_1. Based on the definitions given in Eqs. (9), the black patches ($\mathrm{RP}_{ij} = 1$) in Fig. 6(b) are associated with the low-amplitude oscillation because the distance between two arbitrary points in the time series is smaller than the threshold ε. The white patches ($\mathrm{RP}_{ij} = 0$) arise from the high-amplitude burst oscillation, for which the distance exceeds the threshold ε. Consequently, this global pattern provides an intuitive indication of intrinsic intermittency with a characteristic time scale T_1. However, the local recurrence plot in Fig. 6(c), comprising uniformly distributed black and white stripes, implies a fast-varying time scale T_2 within the high-amplitude periodic oscillation. This time scale was predicted using the low-order thermoacoustic model described in Section 4. A complete model of the intermittent oscillation that accounts for both T_1 and T_2 should incorporate more complex effects, such as the distributed and correlated time delays in hydrocarbon swirl flames [27].

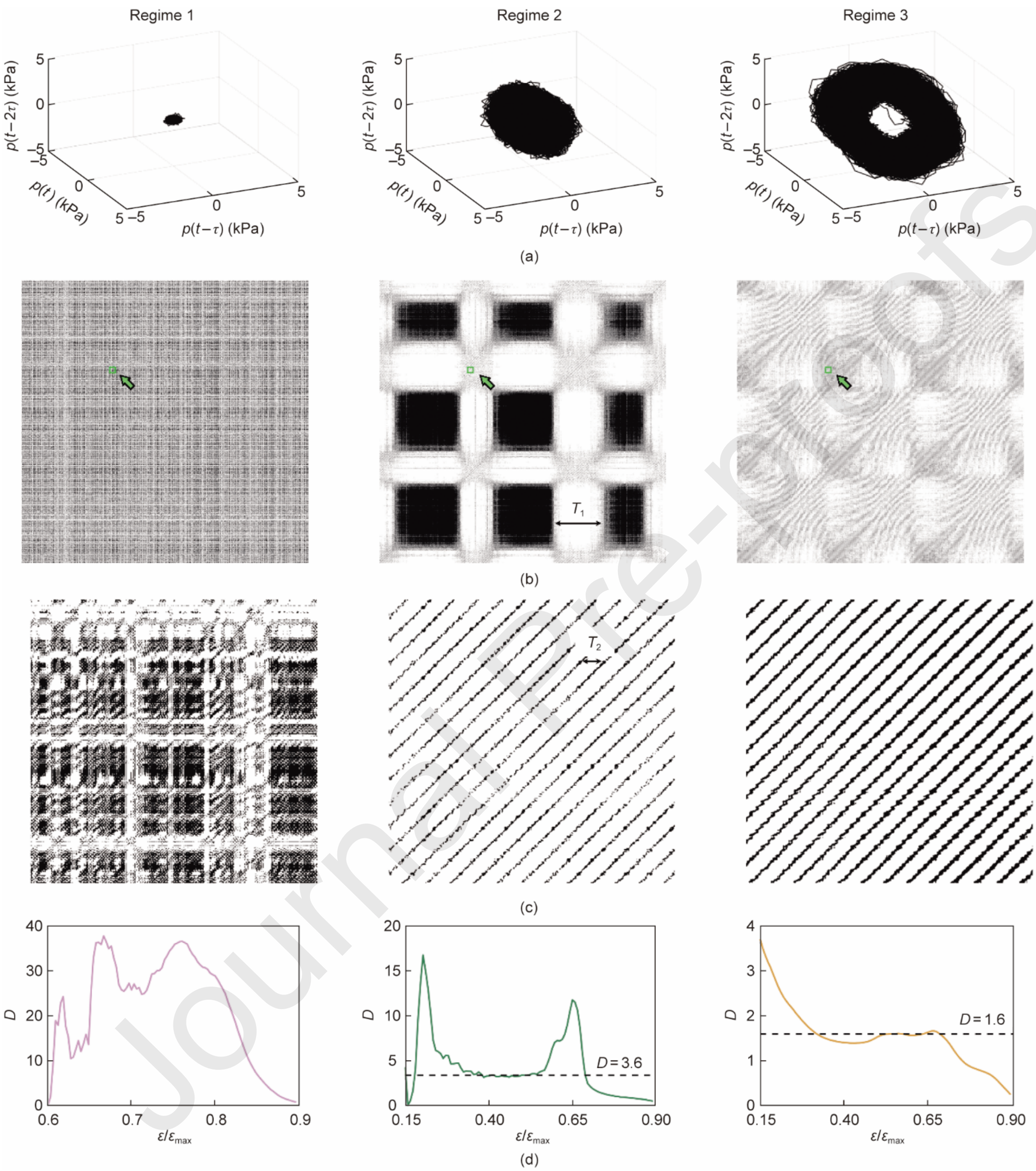

Fig. 6 (a) Phase space reconstruction. (b) Recurrence plot. (c) Zoom view of recurrence plot corresponding to the green box. (d) Dependency of local correlation dimension on the normalized threshold.

In Regime 3, at high equivalence ratios, the pressure fluctuation (marked in orange in Fig. 5) exhibited persistent high-amplitude oscillations. In contrast to the previous regime, the PDF was concave around zero and showed a broad, flat bimodal distribution. A hollow circular orbit is shown in Fig. 6(a). The global recurrence plot in Fig. 6(b) is modified relative to that of Regime 2, whereas the local recurrence plot in Fig. 6(c) remains similar to that in Regime 2. Therefore, the intermittency was substantially attenuated. Fast-varying acoustic oscillations dominated the entire time span, reaching a limit-cycle dynamic state.

Next, we employ the three recurrences quantification metrics introduced in Section 3.2 to highlight the distinctive features of intermittent oscillation relative to limit-cycle oscillation. The recurrence rate RR of Regime 3 has a tighter lower bound of 0 than that of Regime 2 in Fig. 7(a), which physically indicates that the pressure fluctuation in Regime 3 is less affected by intermittent low-amplitude oscillations. The average length l_0 has a higher value when the system spends more time in low-amplitude oscillations. Therefore, the average length decreases significantly during the transition from intermittent oscillation to the limit cycle, as shown in Fig. 7(b). Furthermore, because intermittency serves as a precursor to the detrimental high-amplitude limit-cycle oscillation, real-time monitoring of intermittency using recurrence quantification metrics (e.g., an average length exceeding a given threshold) can provide a warning of impending oscillations [24].

The control system can then be engaged in advance to maintain the observed amplitude at a low level, thereby closing the feedback loop.

As shown in Fig. 6(d), a constant power exponent, that is, the correlation dimension, was observed over a moderate range (marked by a black dashed line) for Regimes 2 and 3. The degeneration of the high-dimensional ($D = 3.6$) phase portrait topological structure of Regime 2 into the low-dimensional ($D = 1.6$) structure of Regime 3 is a significant indication of the thermoacoustic transition, as depicted in Fig. 7(c).

Moreover, for Regime 1, Fig. 7(a) shows that the recurrence rate is independent of the deviation Δ and is strictly bounded between 0.2 and 0.4. The recurrence plot is filled with small-scale structures, resulting in a small average length, as shown in Fig. 7(b). The correlation dimension was considered infinite because convergence was not achieved, as shown in Fig. 6(d).

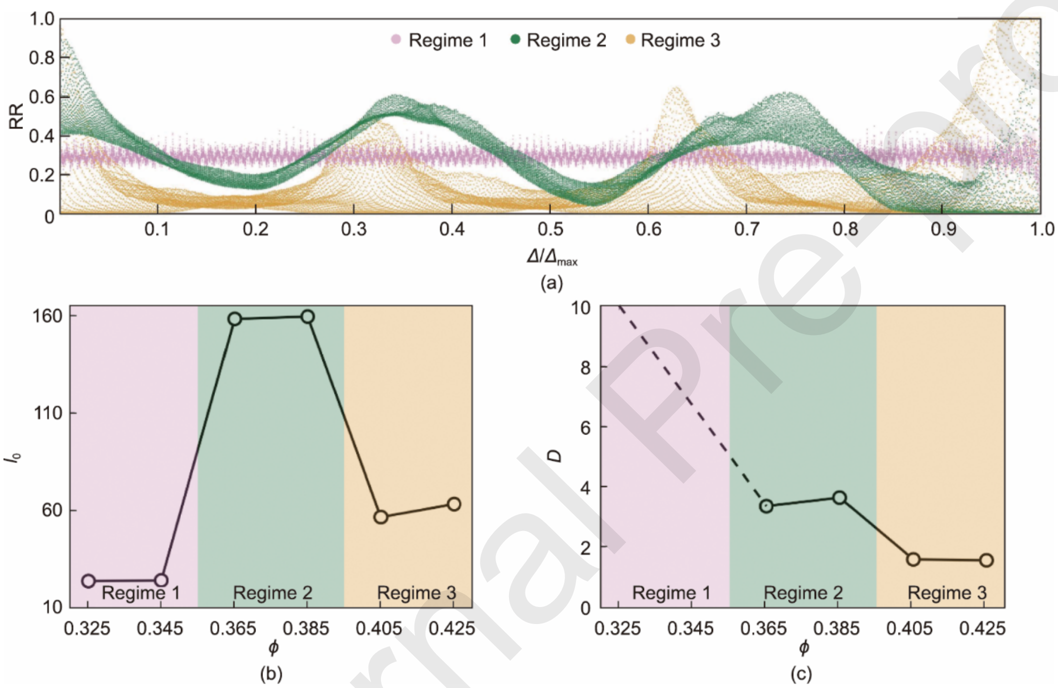

Fig. 7 (a) Scatter plot of recurrence rate RR and normalized deviation $/\Delta_{\min}$. (b) Average length l_0 of the black stripes in the recurrence plot and (c) correlation dimension D of the phase portrait dependency on the equivalence ratio.

5.2. Flame dynamics

We examined flame dynamics to elucidate the mechanism underlying intermittent and limit-cycle oscillations. The phase-averaged flame dynamics of these two types of thermoacoustic oscillations exhibit bulk axial motion over one cycle, as indicated by the green arrows in Fig. 8. The main stage of the hydrogen-arrayed flames periodically lengthens, shrinks, and becomes extinct, leading to coherent unsteady heat-release fluctuations. Flame front merging was also observed (at 180° in Regime 2 and 144° in Regime 3), implying flame–flame interactions. Moreover, the pilot-stage flame angle fluctuated significantly (denoted by the cyan dashed lines in Fig. 8), further contributing to the overall heat-release disturbance.

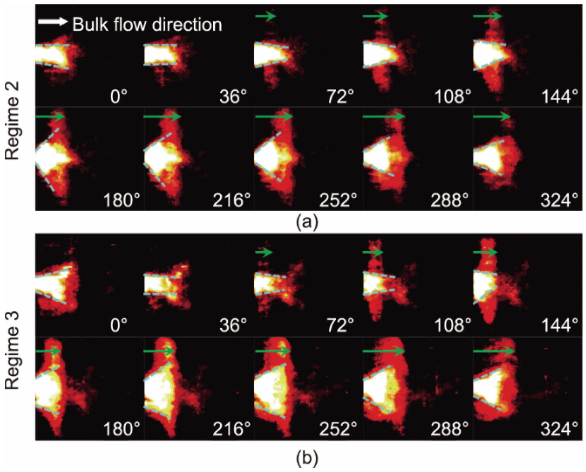

Fig. 8 Phase averaged flame dynamics of the (a) intermittent (Regime 2) and (b) limit-cycle (Regime 3) oscillation.

Next, we analyzed the phase relationships among different flame elements. The flame chemiluminescence image was divided into nine regions according to flame location, as illustrated in Fig. 9. Integration was then performed over each region to obtain the heat-release fluctuation $\dot{q}_i^{'}, i = 1,2,\cdots,9$. $\dot{q}_5^{'}$ represents the heat-release fluctuation of the pilot-stage flame, whereas $\dot{q}_i^{'}$ $(i \neq 5)$ represents the heat-release fluctuation of each individual main-stage flame in the arrayed flame ensemble. The evolution of the phase difference $\Delta\Psi\left(\dot{q}_i^{'},\dot{q}_j^{'}\right)$ between any two flame elements (Region i,j) subjected to a single frequency component was calculated using the wavelet method. Further details regarding this procedure can be found in Ref. [36].

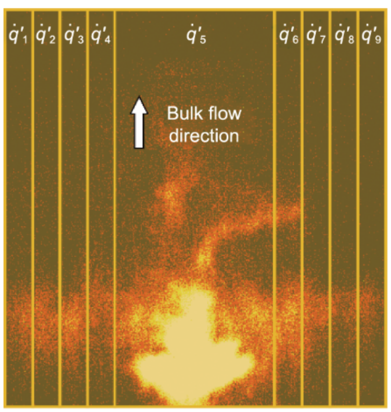

Fig. 9 Illustration of the flame image partition.

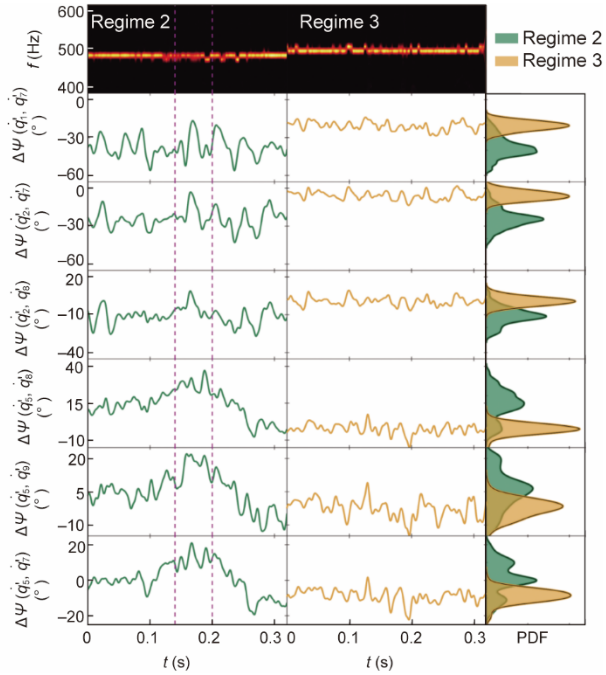

Fig. 10 Time-frequency spectrum, phase difference evolution between two flame elements, and the associated phase angle probability density function of the intermittent (Regime 2) and limit-cycle (Regime 3) oscillation.

The time–frequency spectrum of the global heat-release fluctuation involving all flame elements in Fig. 10 indicates the same dominant fluctuation frequency as the pressure spectrum in Fig. 2. Therefore, we focused on the phase characteristics to determine the thermoacoustic coupling. As shown in Fig. 10, all phase-difference evolutions lie within the in-phase region [−90°, 90°]. Different flame elements oscillated almost synchronously. However, the key distinction between Regimes 2 and 3 lies in the detailed phase-locking behavior. Fig. 10 shows that the phase difference during intermittent oscillation exhibits greater variation than that during limit-cycle oscillation. For example, $\Delta\Psi\left(\dot{q}_1^{'},\dot{q}_7^{'}\right)$ of Regime 2 varies between −16° and −57°, whereas $\Delta\Psi\left(\dot{q}_1^{'},\dot{q}_7^{'}\right)$ in Regime 3 varies between −14° and −29°, corresponding to a phase-variation range that is approximately one-third of that in Regime 2. Furthermore, Fig. 10 shows that the phase-difference angle in Regime 3 has a sharper peak in the probability density distribution, and the overall distribution is closer to a fully synchronized state (0°). In summary, flame elements with poorer phase locking exhibit more pronounced phase fluctuations in heat release, which further perturb the phase difference between pressure and heat-release fluctuations and prevent persistent thermoacoustic coupling. Occasional thermoacoustic decoupling leads to intermittent oscillation. Therefore, the intermittency is attributed to intrinsically modulated phase evolution.

The heat-release fluctuation amplitude is attenuated over a certain interval ((0.14 ± 0.20) s between the purple dashed lines in Fig. 10) in Regime 2, which corresponds to the low-amplitude oscillation and indicates intermittent oscillation. During this interval, a prominent characteristic is that the phase difference between the pilot- and main-stage flame heat release ($\Delta\Psi\left(\dot{q}_5^{'},\dot{q}_i^{'}\right)$ $,i \neq 5$, last three rows in Fig. 10) is higher than that in other intervals, which leads to potential thermoacoustic decoupling. The nominal V-shaped pilot-stage flame and conical main-stage flames exhibited different flame-response characteristics. The destructive interference between the pilot-stage flame-angle fluctuation and the main-stage flame axial oscillation is an important mechanism underlying intermittency. Notably, the reported mesoscale hydrogen-arrayed flame dynamics differ from those of large-scale hydrocarbon swirl flames, in which interference between flame-base angle fluctuation and flame-tip roll-up plays a dominant role [52].

Another possible interpretation of intermittency can be deduced from the thermoacoustic model described in Section 4. As shown in Fig. 4, the growth rate in Regime 2 has a smaller positive margin above zero than that in Regime 3. If physical processes, such as strong turbulent flow, modify key model parameters, such as the time delay, the system may switch between unstable and stable states, resulting in intermittent oscillations.

6. Thermoacoustic-induced structural vibration

The self-sustaining pressure fluctuations induced by thermoacoustic instability continuously impose loading on the combustor's structural components, which may lead to severe engine damage. Therefore, we investigated the structural vibrations induced by thermoacoustic oscillations. Here, we focus only on the operating conditions under which strong pressure fluctuations arise, that is, ϕ = 0.365–0.425 for Regimes 2 and 3.

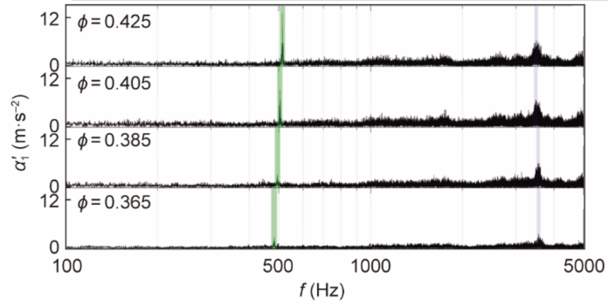

Fig. 11 Axial acceleration spectrum $a_1^{'}$ (x direction). The frequency axis is shown in a logarithmic coordinate.

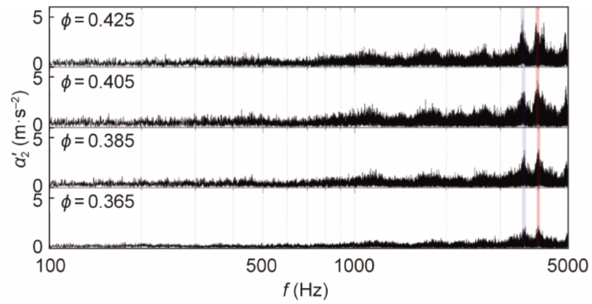

Fig. 12 Transverse acceleration spectrum $a_2^{'}$ (z direction). The frequency axis is shown in a logarithmic coordinate.

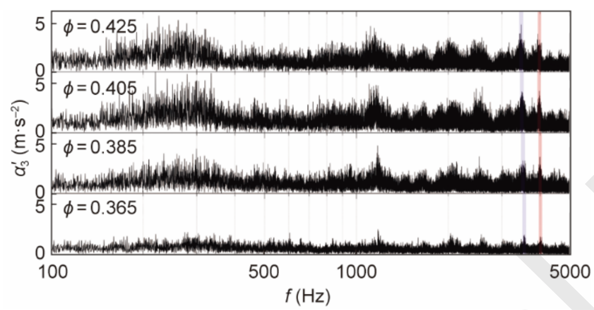

Fig. 13 Transverse acceleration spectrum $a_3^{'}$ (y direction). The frequency axis is shown in a logarithmic coordinate.

The vibration acceleration spectra of the combustor casing in the longitudinal x and transverse y and z directions are shown in Figs. 11–13. The conspicuous peak frequency in the longitudinal acceleration spectrum shown in Fig. 11 (f_1, marked by green bands) coincides with the fundamental acoustic frequency in the pressure spectrum shown in Fig. 2 (also marked by green bands). However, this peak frequency did not appear in the transverse acceleration spectra shown in Figs. 12 and 13. The forced longitudinal vibration, independent of transverse dependence, is attributed to the excitation of the pure longitudinal acoustic mode, as confirmed in Section 4. It can be further inferred that the directionality of the anisotropic thermoacoustic-induced vibration (TIV) is closely related to the acoustic mode properties. In addition, two prominent peak frequencies were observed at approximately 3500 Hz (f_2, marked by blue bands in Figs. 11–13) and approximately 4000 Hz (f_3, marked by red bands in Figs. 12 and 13), which may be related to the structural natural frequencies.

The relationship between the pressure fluctuation amplitude and the longitudinal acceleration fluctuation amplitude at frequency f_1 is shown in Fig. 14. Each data point was calculated from a time series of 0.5 s. Experimental evidence demonstrated that the structural vibration response to acoustic excitation lies within a linear regime. The approximate proportionality coefficient is (8.5 ± 0.4) $\mathrm{m \cdot (s^2 \cdot kPa)^{-1}}$, with 95% confidence. Linear scaling facilitates estimation of the stress level and fatigue life of a structural component, as shown in our previous study [36]. The vibration amplitude induced by intermittent oscillation was generally smaller than that induced by limit-cycle oscillation, indicating that the detrimental effect of intermittency on combustor life was less significant. If the pressure fluctuation amplitude increases further, a nonlinear correction to the acceleration fluctuation amplitude must be introduced.

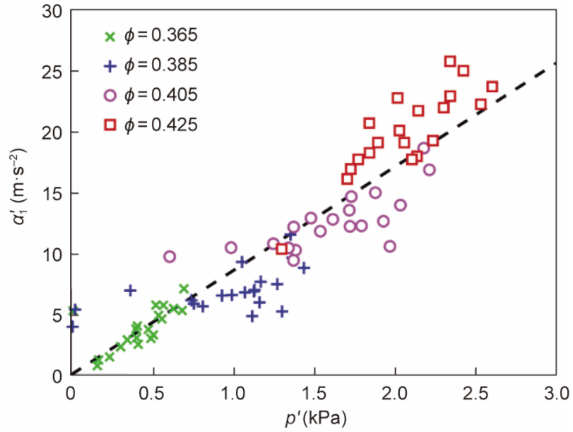

Fig. 14 Scatter plot of the pressure and longitudinal acceleration fluctuation amplitude.

Moreover, we calculated the dimensionless gain transfer from the thermoacoustic oscillations to the structural vibrations as follows:

$$\lambda = \frac{|\hat{a}^{'}/\bar{a}|}{|\hat{p}^{'}/\bar{p}|}, (19)$$

where the hat and bar represent the Fourier-transformed amplitude and the normalization quantity, respectively. Fig. 15 shows that the forced-vibration gain of f_1 is approximately 10^2, whereas the gain of f_2,f_3 is approximately 10^4. TIVs exhibit substantially higher receptivity in the high-frequency regime. This observation is similar to the findings reported in Ref. [34]. If a high-frequency acoustic mode is excited, particularly near the natural structural frequency, the structural vibration amplitude is significantly amplified, leading to severe damage and reduced operational reliability. Therefore, overlap between the frequency band of high structural-response receptivity and the acoustic modal frequency should be avoided in combustor design. Our study also suggests the possibility of detecting thermoacoustic instability using vibration signals without intrusive pressure probes.

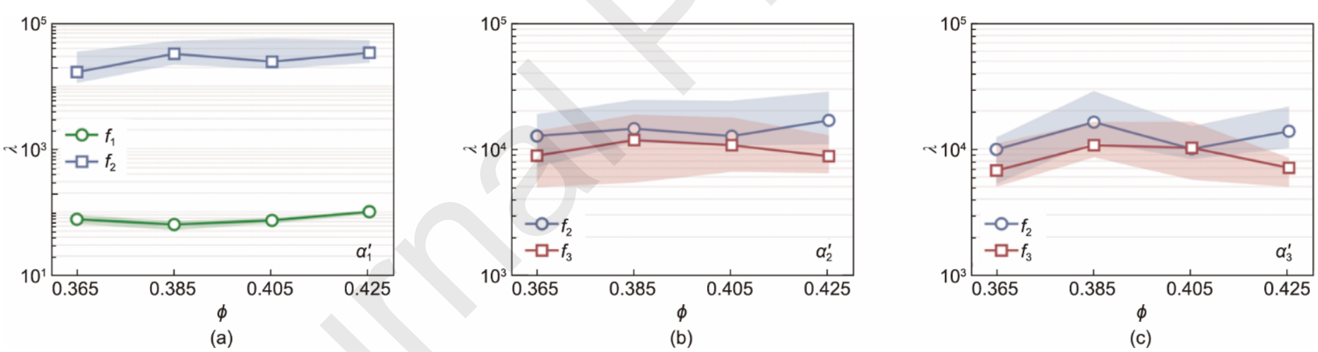

Fig. 15 Acceleration response gain λ of several frequencies. The colored line represents the median value derived from 20 samples. The shaded band indicates the uncertainty, represented by the interquartile range (i.e., interval between the 25% and 75% quartiles). (a) $a_1^{'}$, (b) $a_2^{'}$, and (c) $a_3^{'}$.

7. Conclusions

We investigated the thermoacoustic and structural dynamics of a realistic hydrogen-premixed microtube combustor. The conclusions are as follows:

The longitudinal thermoacoustic instability was successfully captured by the thermoacoustic model. Intermittency, characterized by recurrence quantification metrics (e.g., recurrence rate), serves as an intermediate state during the transition from combustion noise to the limit cycle. The essential dynamic transition mechanism from intermittent to limit-cycle oscillation was attributed to the phase-locking behavior within the arrayed flame ensemble. In a limit-cycle oscillation, the locked phase difference implies well-defined global synchronization within the heat-release distribution, which facilitates robust positive coupling with the acoustics. In contrast, during intermittent oscillation, flame elements exhibiting significant phase-difference fluctuations disrupt the establishment of persistent in-phase coupling between pressure and heat-release fluctuations.

Potential thermoacoustic decoupling gives rise to intermittency, with irregular occurrences of low-amplitude fluctuations. Specifically, the pilot-stage flame-angle fluctuation and the main-stage flame axial oscillation exhibit apparent desynchronization during the low-amplitude phase of intermittent oscillation. The hydrogen-arrayed flame demonstrated coherent flame dynamics distinct from those of the hydrocarbon swirl flame.

TIV is another issue of practical interest. Three primary characteristics were identified. First, TIV is spatially anisotropic and associated with the structure of the forcing acoustic mode. Second, TIV lies within the linear regime, in which the structural vibration amplitude is proportional to the acoustic excitation amplitude. Linear scaling facilitates the definition of the response gain. Third, TIV exhibits high-frequency sensitivity. The vibration response is significantly greater in the high-frequency regime. This study also shows that vibration signals may be valuable for thermoacoustic diagnosis.

The present study can be further extended by involving the engine-relevant elevated-pressure condition and incorporating the nonlinear flame response into the low-order model. The integrated thermoacoustic-structure model is of significance to improve operating safety. They are potential future work directions for the sake of advancing the application of the hydrogen combustor.

CRediT authorship contribution statement

Xiao Han: Conceptualization, Formal analysis, Supervision, Writing- review & editing. **Ziyu Qin:** Formal analysis, Investigation, Methodology, Writing-original draft. **Yuzhen Lin:** Conceptualization, Writing-review & editing. **YunXin Chang:** Validation. **Juan Guzmán-Iñigo:** Writing- review & editing. **Chi Zhang:** Writing-review & editing.

Declaration of completing interest

The authors declare that they have no known competing financial interests or personal relationships that could have appeared to influence the work reported in this paper.

Acknowledgments

This research was funded by the National Natural Science Foundation of China (52476099), the Key Laboratory of Pre-Research Management Center (2023-JCJQ-LB-063-0306), the Fundamental Research Funds for the Central Universities, and the Outstanding Research Project of Shen Yuan Honors College, BUAA (230123208).

References

[1] Wei YM, Chen K, Kang JN, Chen W, Wang XY, Zhang X. Policy and management of carbon peaking and carbon neutrality: a literature review. Engineering (Beijing) 2022;14:52–63.
[2] Pitsch H. The transition to sustainable combustion: hydrogen- and carbon-based future fuels and methods for dealing with their challenges. Proc Combust Inst 2024;40(1–4):105638.
[3] Huang Z. Fuel blend combustion for decarbonization. Proc Combust Inst 2024;40(1–4):105776.
[4] Funke HHW, Beckmann N, Keinz J, Horikawa A. 30 years of dry-low-nox micromix combustor research for hydrogen-rich fuels—an overview of past and present activities. J Eng Gas Turbine Power 2021;143(7):071002.
[5] Funke HW, Beckmann N, Abanteriba S. An overview on dry low nox micromix combustor development for hydrogen-rich gas turbine applications. Int J Hydrogen Energy 2019;44(13):6978–90.
[6] Marek C, Smith T, Kundu K. Low emission hydrogen combustors for gas turbines using lean direct injection. In: Proceedings of the 41st AIAA/ASME/SAE/ASEE Joint Propulsion Conference & Exhibit; 2005 Jul 10–13; Tucson, AZ, USA. Reston: American Institute of Aeronautics and Astronautics (AIAA); 2005. p. 3776.
[7] York WD, Ziminsky WS, Yilmaz E. Development and testing of a low NO_x hydrogen combustion system for heavy-duty gas turbines. J Eng Gas Turbine Power 2013;135(2):022001.
[8] Weiland NT, Sidwell TG, Strakey PA. Testing of a hydrogen dilute diffusion array injector at gas turbine conditions. In: Proceedings of the ASME 2011 Turbo Expo: Turbine Technical Conference and Exposition; 2011 Jun 6–10; Vancouver, BC, Canada. New York City: American Society of Mechanical Engineers (ASME); 2011. p. 1239–47.
[9] Choi J, Rajasegar R, Lee W, Lee T, Yoo J. Hydrogen enhancement on a mesoscale swirl stabilized burner array. Int J Hydrogen Energy 2021;46(46):23906–15.
[10] Moon K, Martin R, Schuermans B, Noiray N. Transfer functions of lean fully-and technically-premixed jet-stabilized turbulent hydrogen flames. Proc Combust Inst 2024;40(1–4):105256.
[11] Jin U, Kim KT. Experimental investigation of combustion dynamics and nox/co emissions from densely distributed lean-premixed multinozzle $CH_4/C_3H_8/H_2$/air flames. Combust Flame 2021;229:111410.
[12] Kang H, Lee T, Jin U, Kim KT. Experimental investigation of combustion instabilities of a mesoscale multinozzle array in a lean-premixed combustor. Proc Combust Inst 2021;38(4):6035–42.
[13] Poinsot T. Prediction and control of combustion instabilities in real engines. Proc Combust Inst 2017;36(1):1–28.
[14] Candel S, Durox D, Schuller T, Bourgouin JF, Moeck JP. Dynamics of swirling flames. Annu Rev Fluid Mech 2014;46(1):147–73.
[15] O'Connor J. Understanding the role of flow dynamics in thermoacoustic combustion instability. Proc Combust Inst 2023;39(4):4583–610.
[16] Morgans AS, Yang D. Thermoacoustic instability in combustors. Annu Rev Fluid Mech 2025;57:9–13.
[17] Lee T, Kim KT. Combustion dynamics of lean fully-premixed hydrogen-air flames in a mesoscale multinozzle array. Combust Flame 2020;218:234–46.
[18] Kang H, Kim KT. Combustion dynamics of multi-element lean- premixed hydrogen-air flame ensemble. Combust Flame 2021;233:111585.
[19] Durocher A, Fan L, Füri M, Bourque G, Bergthorson JM, Yun S, et al. Phase-averaged, 3D OH-LIF reconstruction for multi-nozzle, micromixed hydrogen combustion. Proc Combust Inst 2024;40:105561.

[20] Æsøy E, Aguilar JG, Wiseman S, Bothien MR, Worth NA, Dawson JR. Scaling and prediction of transfer functions in lean premixed H_2/CH_4-flames. Combust Flame 2020;215:269–82.
[21] Garcia AM, Le Bras S, Prager J, Haringer M, Polifke W. Large eddy simulation of the dynamics of lean premixed flames using global reaction mechanisms calibrated for CH_4–H_2 fuel blends. Phys Fluids 2022;34(9):34.
[22] Kang H, Yoon C, Kim KT. Experimental and numerical investigations of forced response of multi-element lean-premixed hydrogen flames. Combust Flame 2023;258:113079.
[23] Guan Y, Gupta V, Li LK. Intermittency route to self-excited chaotic thermoacoustic oscillations. J Fluid Mech 2020;894:R3.
[24] Nair V, Thampi G, Sujith R. Intermittency route to thermoacoustic instability in turbulent combustors. J Fluid Mech 2014;756:470–87.
[25] Kabiraj L, Sujith RI. Nonlinear self-excited thermoacoustic oscillations: intermittency and flame blowout. J Fluid Mech 2012;713:376–97.
[26] Roy A, Singh S, Nair A, Chaudhuri S, Sujith RI. Flame dynamics during intermittency and secondary bifurcation to longitudinal thermoacoustic instability in a swirl-stabilized annular combustor. Proc Combust Inst 2021;38(4):6221–30.
[27] Bonciolini G, Faure-Beaulieu A, Bourquard C, Noiray N. Low order modelling of thermoacoustic instabilities and intermittency: flame response delay and nonlinearity. Combust Flame 2021;226:396–411.
[28] Bhavi RS, Pavithran I, Roy A, Sujith R. Abrupt transitions in turbulent thermoacoustic systems. J Sound Vibrat 2023;547:117478.
[29] Lee M. Coupling and synchronisation effects on local lock-in of two thermoacoustic oscillators in a stochastic environment. J Fluid Mech 2025;1017:R2.
[30] Lieuwen TC, Yang V. Combustion instabilities in gas turbine engines: operational experience, fundamental mechanisms, and modeling. Reston: The American Institute of Aeronautics and Astronautics, Inc.; 2005.
[31] Pozarlik AK, Kok JB. Fluid-structure interaction in combustion system of a gas turbine—effect of liner vibrations. J Eng Gas Turbine Power 2014;136(9):091502.
[32] Shahi M, Kok JB, Roman Casado JC, Pozarlik AK. Strongly coupled fluid–structure interaction in a three-dimensional model combustor during limit cycle oscillations. J Eng Gas Turbine Power 2018;140(6):061505.
[33] Xia Y, Sharkey P, Verma I, Khaware A, Cokljat D. Prediction of thermoacoustic instability and fluid–structure interactions for gas turbine combustor. J Eng Gas Turbine Power 2022;144(9):091005.
[34] Can Altunlu A, van der Hoogt PJ, de Boer A. Sensitivity of combustion driven structural dynamics and damage to thermo-acoustic instability: combustion-acoustics-vibration. J Eng Gas Turbine Power 2014;136(5):051501.
[35] Rubio-Rubio M, Veiga-López F, Martínez-Ruiz D, Fernández-Tarrazo E, Sánchez-Sanz M. Suppression of thermoacoustic instabilities by flame-structure interaction. Proc Combust Inst 2023;39(2):1577–85.
[36] Qin Z, Lin Y, Han M, Han X, Zhang X, He P, et al. Experimental and theoretical investigation on the thermoacoustic-induced vibration in a centrally-staged combustor. Combust Flame 2025;273:113890.
[37] Qin Z, Song H, Han X, Li L, Lin Y, Xu L. Fuel stratification effects on thermoacoustic instability for swirl spray flame in an aero-engine centrally-staged combustor. Aerosp Sci Technol 2025;161:110163.
[38] Schuller T, Durox D, Palies P, Candel S. Acoustic decoupling of longitudinal modes in generic combustion systems. Combust Flame 2012;159(5):1921–31.
[39] Han X, Laera D, Yang D, Zhang C, Wang J, Hui X, et al. Flame interactions in a stratified swirl burner: flame stabilization, combustion instabilities and beating oscillations. Combust Flame 2020;212:500–9.
[40] Abarbanel HD, Brown R, Sidorowich JJ, Tsimring LS. The analysis of observed chaotic data in physical systems. Rev Mod Phys 1993;65(4):1331–92.
[41] Kennel MB, Brown R, Abarbanel HD. Determining embedding dimension for phase-space reconstruction using a geometrical construction. Phys Rev A 1992;45(6):3403–11.
[42] Marwan N, Romano MC, Thiel M, Kurths J. Recurrence plots for the analysis of complex systems. Phys Rep 2007;438(5–6):237–329.
[43] Kantz H, Schreiber T. Nonlinear time series analysis. Cambridge: Cambridge University Press; 2003.
[44] Grassberger P, Procaccia I. Characterization of strange attractors. Phys Rev Lett 1983;50(5):346–9.
[45] Hernandez-Rivera R, Troiani G, Pagliaroli T, Hernandez-Guerrero A. Detection of the thermoacoustic combustion instabilities of a slot burner based on a diagonal-wise recurrence quantification. Phys Fluids 2019;31(12):31.
[46] Dowling AP. Nonlinear self-excited oscillations of a ducted flame. J Fluid Mech 1997;346:271–90.
[47] Durox D, Schuller T, Noiray N, Candel S. Experimental analysis of nonlinear flame transfer functions for different flame geometries. Proc Combust Inst 2009;32(1):1391–8.
[48] Schuller T, Durox D, Candel S. A unified model for the prediction of laminar flame transfer functions: comparisons between conical and v-flame dynamics. Combust Flame 2003;134(1–2):21–34.
[49] Polifke W, Lawn C. On the low-frequency limit of flame transfer functions. Combust Flame 2007;151(3):437–51.
[50] Li J, Morgans AS. Time domain simulations of nonlinear thermoacoustic behaviour in a simple combustor using a wave-based approach. J Sound Vibrat 2015;346:345–60.
[51] Rayleigh L. The explanation of certain acoustical phenomena. Nature 1878;18(455):319–21.
[52] Palies P, Durox D, Schuller T, Candel S. The combined dynamics of swirler and turbulent premixed swirling flames. Combust Flame 2010;157(9):1698–717.

Declaration of Interest Statement

☒ The authors declare that they have no known competing financial interests or personal relationships that could have appeared to influence the work reported in this paper.

☐ The author is an Editorial Board Member/Editor-in-Chief/Associate Editor/Guest Editor for this journal and was not involved in the editorial review or the decision to publish this article.

☐ The authors declare the following financial interests/personal relationships which may be considered as potential competing interests: